KSME

Springer

Journal of Mechanical Science and Technology 35 (7) 2021

Original Article
DOI 10.1007/s12206-021-0632-y

Keywords:
· Unmanned aerial vehicle
· Propeller
· Numerical method
· Aerodynamic simulation
· Structural analysis
· Fluid-structure interaction

Correspondence to:
Zhen Qin
zhen.qin@gnu.ac.kr;
Sung-Ki Lyu
sklyu@gnu.ac.kr

# These authors equally contributed to this work as first author.

Citation:
Wu, Y.-T., Qin, Z., Eizad, A., Lyu, S.-K. (2021). Numerical investigation of the mechanical component design of a hexacopter drone for real-time fine dust monitoring. Journal of Mechanical Science and Technology 35 (7) (2021) 3101~3111.
http://doi.org/10.1007/s12206-021-0632-y

Received November 25th, 2020
Revised April 5th, 2021
Accepted April 12th, 2021

† Recommended by Editor Hyung Wook Park

Numerical investigation of the mechanical component design of a hexacopter drone for real-time fine dust monitoring

Yu-Ting Wu[1,#], Zhen Qin[1,#], Amre Eizad[2] and Sung-Ki Lyu[1]

[1]School of Mechanical and Aerospace Engineering, Gyeongsang National University, 501 Jinju-daero, Jinju-si, Gyeongsangnam-do 52828, Korea, [2]School of Integrated Technology, Gwangju Institute of Science and Technology, 123 Cheomdangwagi-ro, Buk-gu, Gwangju 61005, Korea

Abstract Multi-rotor unmanned aerial vehicles (UAVs) are being widely used in various military and civilian fields because they can replace manned systems in the performance of a variety of difficult and/or hazardous tasks. Various UAV designs have been developed to fulfill the requirements of various applications. The current work investigates the design of a hexacopter drone with foldable arms to support the six propulsion units that is designed for real-time fine dust monitoring. The propeller and foldable arm are the key mechanical power transmission components in this design, so their propulsion performance and safety reliability have been numerically investigated in this research. The finite volume method (FVM) based aerodynamic characteristics simulation is utilized to calculate and observe the operational performance of eight different proposed propeller blade designs. The optimal design was obtained through a series of comparisons of the simulation outcomes. The flow field force acting on the propeller blade was analyzed using the fluid-structure interaction (FSI) based simulation method. In addition, the design philosophy of using carbon fiber composite material to replace the traditional aluminum alloy in the manufacture of the foldable arm is presented. The rationality of this design philosophy is verified through finite element method (FEM) based structural analysis. The design experience gained from this study provides a theoretical basis for the development of components for multi-rotor UAVs.

1. Introduction

A drone is an unmanned aerial vehicle (UAV) that is operated by radio remote control equipment and its own programed control device [1]. As a product of the integration of aeronautical and electronic technologies, the main role of drones is to do away with the requirement for human presence in performing difficult or dangerous tasks [2-4]. With many advantages such as low cost, small size and convenient use, UAVs are being greatly used in military and civilian applications [5, 6]. In military use, drones can replace humans in performing tasks such as reconnaissance, fire support, search and rescue, etc. In civilian use, drones are employed mainly in aerial photography, bridge inspection, pesticide spraying, monitoring of environmental pollutants, etc. Recent research predicts that by 2021, the global drone market is expected to grow to 19.85 billion US dollars, with a compound annual growth rate (CAGR) of nearly 13 % during the forecast period [7].

The size, endurance and functional requirements for drones vary according to their different working conditions [8, 9]. The design of drones needs to take into account the required package, aerodynamics, aeroelasticity, structure, propulsion, stability, electronic control, manufacturing, acoustics etc. [10-14]. This is a complex interdisciplinary task that requires a great amount of effort to be put into the design of UAVs [15-19].

Eleni et al. [20] carried out a numerical simulation of the National Advisory Committee for Aeronautics (NACA) 0012 airfoil. They summarized the characteristics of the airfoil in response to various angles of attack and analyzed the stall conditions. Zhu et al. [21] used computational

fluid dynamics (CFD) to design and evaluate the aerodynamic efficiency of octocopter drones, and outlined an aerodynamic efficiency and performance-enhancing methodology based on optimized configuration of a hybrid octocopter drone. A novel design method for the fixed blade MAV (micro air vehicle) was presented by Hassanalian et al. [22], and the results of simulations based on the XFLR5 airfoil was discussed. Through repeated optimizations, efficiency was improved and the design costs were reduced. It has been observed that in order to save manufacturing time and design costs, numerical investigation methods have become a mainstream tool for verifying the preliminary designs of complex systems such as UAVs [23-28].

This research will introduce the design and optimization method for a real-time fine dust monitoring hexacopter drone. CFD (computational fluid dynamics) simulation software is used to verify the proposed propeller blade designs and to obtain the optimal solution and the FSI (fluid structure interaction) method is employed to verify the structural stability of the selected blade design. The hexacopter design includes foldable arms for mounting the propulsion units. For these arms, a weight optimization by using carbon fiber composite material instead of the conventional alloy material is proposed. The feasibility of this proposition is discussed through the structural analysis based comparison of the two designs.

As a result, the optimal design for the hexacoptor is proposed after a series of numerical investigations of eight different designs. Moreover, the aerodynamic characteristics of the selected design and the structural strength of the lightweight folding arm design are validated utilizing different methods.

2. Evaluation methods and parameters

Hexacopter drones are widely used in pesticide spraying, environmental monitoring, aerial photography and many other fields [29-31]. This article presents a series of numerical investigations that have been carried out to validate the design of a hexacopter drone for real-time fine dust monitoring.

2.1 Propeller design evaluation and selection

Hexacopters generally employ propellers to gain lift and thrust. Propellers generate lift by discharging the air around the blades backwards through their rotating motion. This movement principle is also called air reaction movement. Many factors, such as the diameter of the propeller, the number of blades, the airfoil design, the width and thickness of the blades, the installation twist angle, etc., affect the performance of propellers.

In this research, taking into account the UAV's maximum takeoff weight (mainly comprised of the weight of the real-time dust monitoring device and the weight of the drone), flight altitude, operating environment and other factors, the diameter of the propeller is set as 600 mm and the number of blades is set as two.

The shape and size of the airfoil has a direct effect on the performance of the propeller (lift, drag, etc.) [32]. Commonly used propeller airfoils include the NACA airfoil designed by the National Advisory Committee for Aeronautics of the United States, the NAГN airfoil of the Soviet Central Fluid Research Institute, the British RAF-6 airfoil and the ARA-D airfoil [33]. The NACA four-digit airfoils are widely used in the UAV industry due to their high maximum lift coefficient and low drag coefficient. In this study, several different NACA airfoils are evaluated.

In this paper, the control variable method is used to investigate eight groups of different propeller blade designs. The main variables are the installation twist angle (W), the height (H) between the starting point of the chord on the leading edge of the airfoil and the reference plane, the maximum camber (C) and the thickness (TH) of the of airfoil. The curves W1, W2 and W3 shown in Fig. 1(a) represent respectively the design comparison of three different installation twist angles along the radius. W1 has the largest twist angle at the root of the blade that gradually decreases along the radius. The maximum twist angle of W2 is same to W1, but the position of maximum of W2 is shifted to 0.23 r/R. W3 has the same position of maximum twist as W2, but the maximum twist angle is about half of W2. In order to observe the effects of the height between the starting point of the chord on the leading edge of the airfoil and the reference plane on the performance of the propeller, three variables are set as shown in Fig. 1(b). H1 implies that there is no height difference from the reference plane along the radius, while H2 and H3 respectively indicate two different height designs where H3 has a larger change.

Figs. 1(c) and (d) represent design variables of the maximum camber and thickness that directly affect the shape of the airfoil along the blade radius. The combination matrix with different variables of the eight propeller designs is shown in Table 1.

Traditional experimental verification methods may incur a high cost and require a long testing time. Therefore, in this study we have utilized the commercial numerical simulation software ANSYS Workbench and Fluent release 2019R3 to calculate and observe aerodynamic characteristics of the flow field, pressure field, etc., around the propeller. The air used in the simulation is assumed as incompressible and conforming to the Reynolds averaged Navier-Stokes (RANS) equations. Eqs. (1) and (2) are the continuous and momentum conservation equations.

$$\nabla \cdot \vec{v} = 0 , \tag{1}$$

$$\rho \frac{\partial}{\partial t}(\vec{v}) + \rho \nabla \cdot (\vec{v}\vec{v}) = -\nabla p + \nabla \cdot \left(\bar{\bar{\tau}}\right) + \vec{F} . \tag{2}$$

Here, $\bar{\bar{\tau}} = \mu \left[\left(\nabla \vec{v} + \nabla \vec{v}^{T} \right) - \frac{2}{3} \nabla \cdot \vec{v} I \right]$

where t denotes time, ρ is the density, P is the static pressure, $\bar{\bar{\tau}}$ is the Reynolds stress tensor, F is the body force or momentum source term, v is the velocity vector in the inertial coordinate system, μ is the viscosity coefficient and I is the unit tensor.

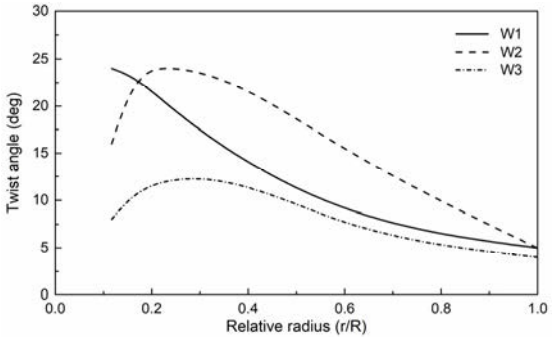

(a) Twist angle

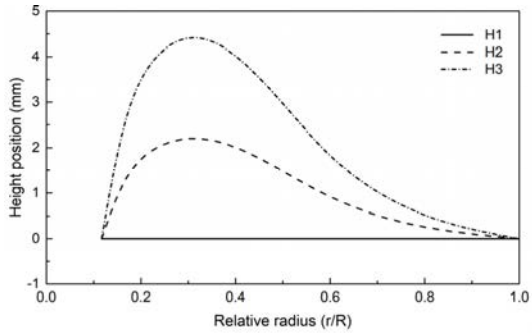

(b) Height difference between the starting point of the chord on the leading edge of the airfoil and the reference plane

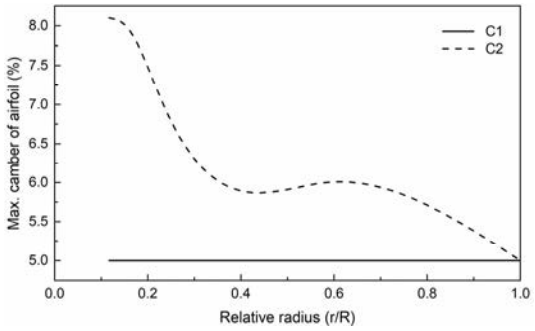

(c) Maximum camber of the airfoil

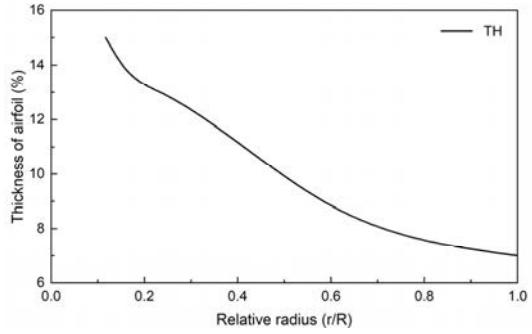

(d) Thickness of the airfoil

Fig. 1. Different design variables along the radial direction of the propeller blade.

The turbulence model in the numerical investigation was selected as SST K-omega (SST k-ω), which predicts the far field and near wall results based on K-epsilon (k-ε) and k-ω models, respectively [34]. It has been reported that the SST k-ω is the most appropriate of the three commonly used turbulence models (Spalart-Allmaras, realizable k-ε and SST k-ω) to deal with bodies such as airfoils [35]. The SIMPLE (semi-implicit method for pressure-linked equations) method is generally used to solve the momentum and continuous equations simultaneously [36, 37]. For the boundary conditions, as shown in Fig. 2(a), velocity inlet and pressure outlet are used in the simulation. Considering the power performance of the propeller driving motors and the working characteristics of real-time monitoring of fine dust, the rotation speed of the propeller is set to 6000 rpm.

Table 1. Combination matrix with different design variables of propeller design.

Desing No.	Twist angle	Height	Max. camber
1	W1	H1	C1
2	W2	H2	C1
3	W1	H1	C2
4	W2	H2	C2
5	W3	H2	C1
6	W3	H3	C1
7	W1	H2	C1
8	W1	H2	C2

As the propeller is a rotating component, the grid of the propeller should also follow the rotations in the simulation. Therefore, comparing with the dynamic mesh method, the mesh motion can obtain accurate results while saving computing time. As shown in Fig. 2(b), the computational domain is divided into two parts: the stationary domain and the rotating domain. The mesh type used is unstructured mesh, which is determined by the complexity of the propeller geometry. The optimal grid after mesh-independence study is applied in this research.

In addition, in order to obtain the best lightweight solution for the hexarotor drone, the material of the propeller blades was defined as carbon fiber composite instead of the traditional alloy material. FSI simulation based on the integration of FVM (finite volume method) and FEM (finite element method) was used to analyze the influence of the fluid load on the structural stability and design feasibility of the propeller at high rotational speed [18, 38-40].

2.2 Foldable arm evaluation method

The foldable arm is an important part that connects the propeller and the center frame. When the drone is in operation, the lift generated by the propeller is applied to one end of the arm while the other end carries its share of the weight of the drone and the UAV's payload. In order to make the drone easy to carry, the arms can be folded as shown in Fig. 3.

Considering the important role the arm plays in power transmission, its rod is generally made of a rigid metal alloy like steel or aluminum alloy. For the movable parts, plastic materials with

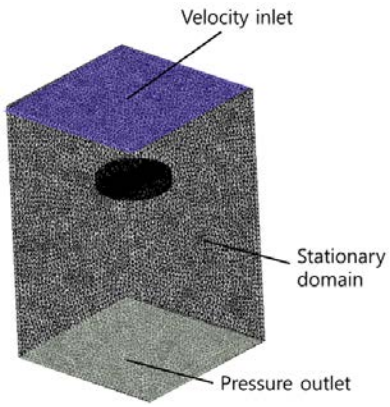

(a) Boundary conditions

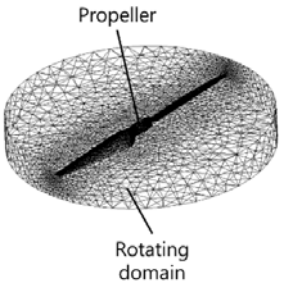

(b) Propeller and the rotating domain

Fig. 2. Mesh and boundary conditions of for the CFD simulation.

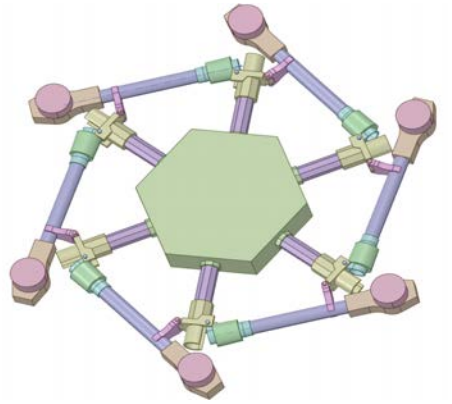

(a) The arms in folded condition

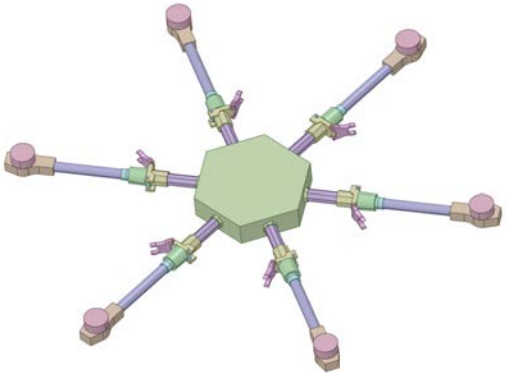

(b) The arms in expanded condition

Fig. 3. 3D modeling of the foldable arm design.

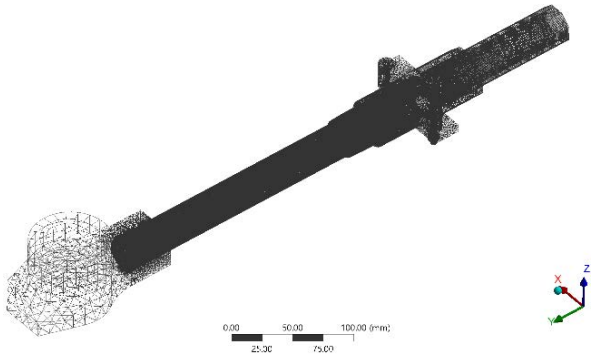

(a) The generated mesh

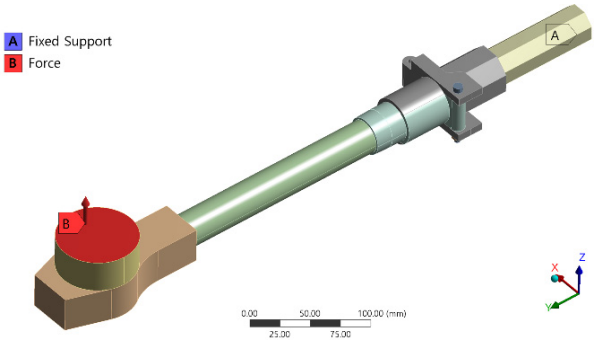

(b) The boundary conditions

Fig. 4. Mesh and boundary conditions used for the structural analysis.

a certain of degree of plasticity are generally used to meet the requirements of repeated folding. In recent years, composite material technology has developed rapidly. Carbon fiber, with its relatively light-weight and high tensile strength, has gradually replaced traditional metallic materials in many industrial applications. In this study, in order to obtain the optimal weight of the drone, we have attempted to replace the metallic rod of the foldable arm with one made of carbon fiber composite material. Meanwhile, FEM based structural analysis was utilized to evaluate the structural stability of this new design philosophy. In addition, as a comparison, the simulation of the traditional (metallic) foldable arm was also carried out.

Considering the simulation duration and the structural symmetry of the hexarotor UAV, only one foldable arm was analyzed in this research. Figs. 4(a) and (b), respectively, show the mesh structure and boundary conditions used in the simulation. To ensure good convergence and simulation results, the mesh of the main parts under investigation was kept quite fine, as shown in the figure [41]. The maximum lift generated by the rotation of the propeller (the safety factor has already been taken into account) is applied to the position of the motor (to the left in Fig. 4(b)), and the end connected to the center frame is fixed (to the right in Fig. 4(b)).

A series of simulations were carried out on the propeller blade and foldable arm using the investigation methods described in this section. The results of these simulations are presented and discussed in the following sections with the objective of obtaining an optimal set of design parameters.

Table 2. Performance characteristics of the eight blade designs obtained through CFD simulation.

Design no.	Thrust force [N]	Moment [N·m]
1	48.80	2.05
2	95.20	4.22
3	56.00	2.40
4	102.20	4.66
5	38.30	1.70
6	38.00	1.69
7	48.12	2.03
8	54.90	2.39

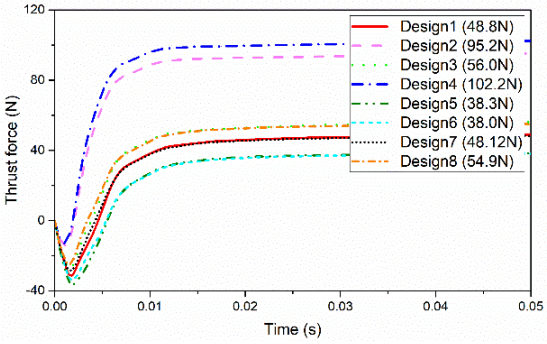

Fig. 5. Comparison of the thrust output obtained from the eight blade designs.

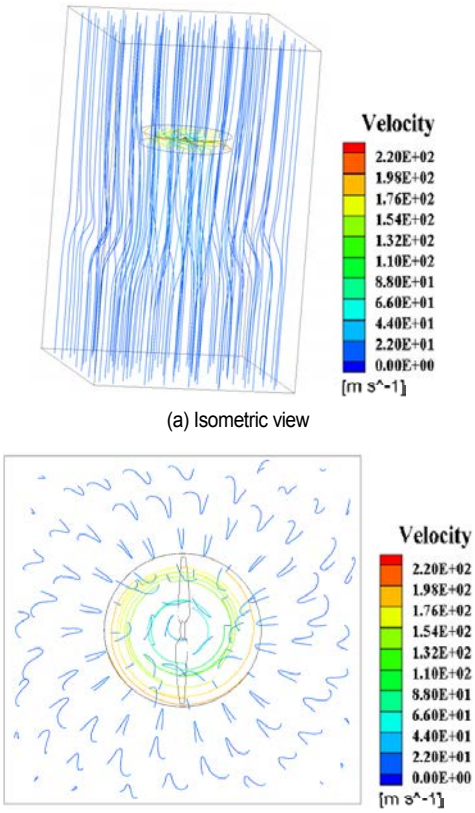

(a) Isometric view

(b) Top view

Fig. 6. The velocity streamline when the propeller blades are rotating steadily.

3. Results and discussion

3.1 Aerodynamic simulation of the propeller blade design

We carried out a series of CFD simulations on eight different of propeller designs consisting of eight different blade airfoil designs. The performance results obtained from these simulations are summarized in Fig. 5 and Table 2.

Design 1 and design 3 have the same air foil twist angle (W1) and height (H1); however design 3 uses the C2 airfoil camber. The stable thrust supplied by design 3 is 56 N, which is about 15 % higher than design 1 using the C1 airfoil camber. In addition, the torque required by design 3 is 17 % higher than that required by design 1. It can be concluded that the propeller with the greater airfoil camber (C2) can provide the higher thrust, but it requires more torque to operate. This conclusion is verified by the comparison of design 2 with design 4 and of design 7 with design 8.

Design 1 and design 7 have the same twist angle (W1) and maximum camber (C1) of the airfoil. However, they vary in terms of the height (H) between the starting point of the chord on the leading edge of the airfoil and the reference plane with design 1 having height H1 and design 7 having height H2. Nonetheless, the results show that the thrust output and torque requirement do not differ greatly between the two designs. This conclusion is verified by the comparison of design 3 with design 8 and of design 5 with design 6.

Design 2, design 5 and design 7 have different twist angles (W). From the comparison of design 2 and design 7, it can be seen that the thrust output obtained with W2 is nearly 1.5 times higher than that obtained with W3, while the torque requirements of the two designs also show a similar relationship. In other words, although both the designs have similar propulsion efficiencies, the design with a larger twist angle can produce greater lift. Through comparison of the propulsion performance of designs 2 and 7, it can be seen that the design with the greater twist angle (W2) that is slightly offset in the radial direction of the blade can provide a greater thrust than the design with the lesser (W1) and gradually decreasing twist angle along the radial direction. The comparison of designs 4 and 8 verifies the correctness of this conclusion. Based on the simulation outcomes and considering the takeoff weight and working conditions of the hexarotor drone, design 2 was selected as the optimal design since it meets our propulsion performance requirements and has a higher propulsion efficiency than the other designs.

After selection of the optimal design, aerodynamic characteristics of the propeller with design 2 blades were analyzed. Fig. 6 shows the velocity streamline when the propeller blades are rotating steadily. It can be seen that the air entering from the inlet is drawn in to the blade area where it rotates with the propeller and then proceeds towards the outlet. The air velocity

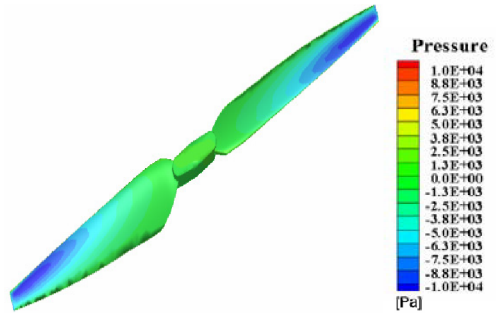

(a) Top surface

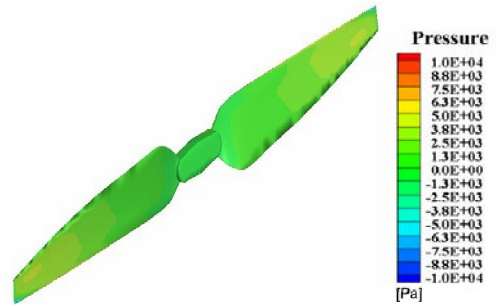

(b) Bottom surface

Fig. 7. Pressure contour of the flow field acting on the propeller.

inside the rotating area of the propeller blade is significantly higher than that in the outer area. This can be intuitively observed from Fig. 6(b).

The pressure contour of the flow field acting on the propeller is shown in Fig. 7. It can be observed that the pressure on the bottom side of the propeller is significantly higher than the pressure on the top side, and it increases along the radial direction from the blade root to the tip. The pressure difference between the top surface and the bottom surface of the blade generates the lift needed to make the drone fly.

In order to observe the pressure distribution of the flow field around the propeller, the middle surface of the propeller was intercepted and the result obtained is shown in Fig. 8. It can be seen that the pressure near the upper surface of the propeller is significantly lower than that under the lower surface, and shows a decreasing trend from the root of the blade to the tip. These results show that the thrust generated by the propeller blades is mainly produced in the middle and tip part of the blade under the simulated working conditions.

Figs. 9(a)-(c) show respectively the pressure contours of the airfoil at r/R = 0.23, 0.58, and 0.99. It can be seen that the maximum pressure value of 7.35×10^3 Pa appears at r/R = 0.99, which is closer to the blade tip. Thus, the closer to the blade root the lower is the maximum pressure around the airfoil. The position where the maximum pressure appears differs slightly with the twist angle. Moreover, there is a negative pressure region on the top of the airfoil, which indicates that the blade is being sucked upwards by the air flowing over the top. Through comparison of the pressure values observed in this simulation, it can be concluded that the negative pressure generated on

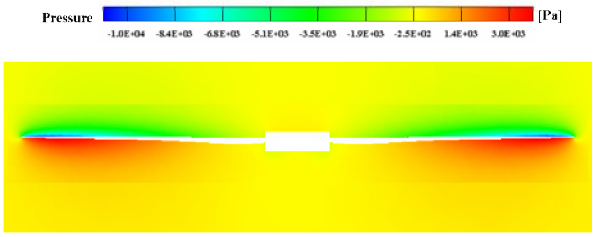

Fig. 8. Pressure contour at the middle section of the propeller.

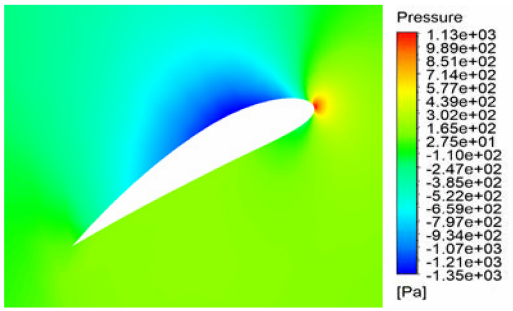

(a) r/R = 0.23

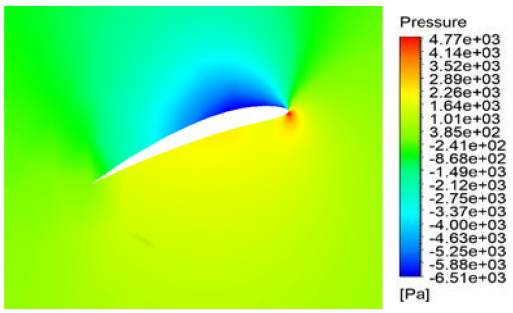

(b) r/R = 0.58

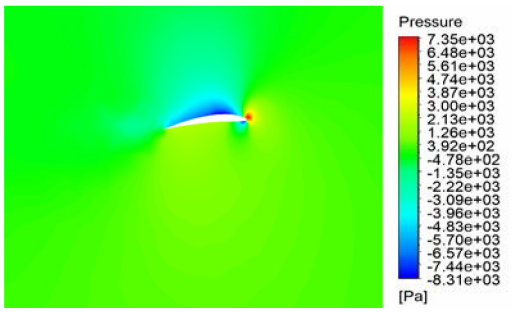

(c) r/R = 0.99

Fig. 9. Pressure contours of the airfoil at different r/R values.

the top surface of the propeller contributes more to lift generation than the high pressure generated on the bottom surface.

Figs. 10(a)-(c) show the air velocity contours and vector distribution around the airfoil at r/R = 0.23, 0.58, and 0.99, respectively. It can be clearly seen that the maximum velocities of the flow fields around all the airfoils appear at the trailing edge. By comparing the airflow vectors around the airfoils, it can be observed that the airflow at r/R = 0.58 has a large deviation near

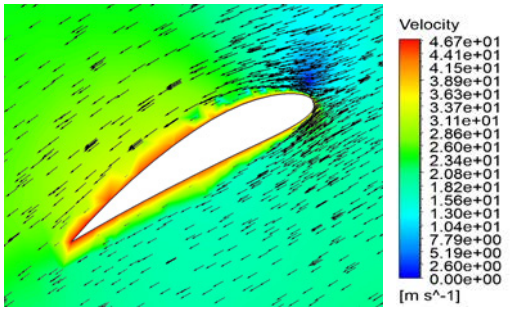

(a) r/R = 0.23

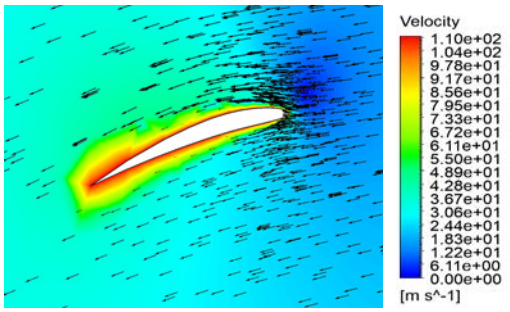

(b) r/R = 0.58

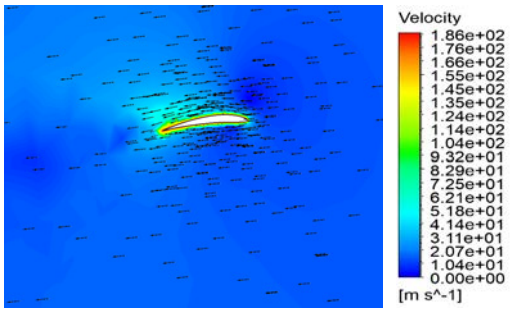

(c) r/R = 0.99

Fig. 10. Air velocity contours and vector distribution around the airfoil at different r/R values.

the upper part of the leading edge. However, this phenomenon was not found around the airfoils at r/R = 0.23 and r/R = 0.99. This shows that the design of this propeller blade can cope with a greater angle of attack while effectively avoiding a stall condition.

In order to observe the influence of the force generated by the flow field on the structural stability of the propeller, the data about pressure on the blade obtained using CFD was imported into the FEM module and the structural analysis was carried out. The results of this analysis are shown in Fig. 11.

From the deformation distribution results shown in Fig. 11(a), it can be observed that, as expected, the maximum deformation appears at the tip of the blade. The maximum deformation value of 3.5 mm is acceptable for carbon fiber materials as they have a high recovery elasticity. Fig. 11(b) shows the stress distribution in the propeller. It can be seen that the maximum stress occurs at the root of the blade. This is the reason why a thicker airfoil design is generally used at the root of propeller

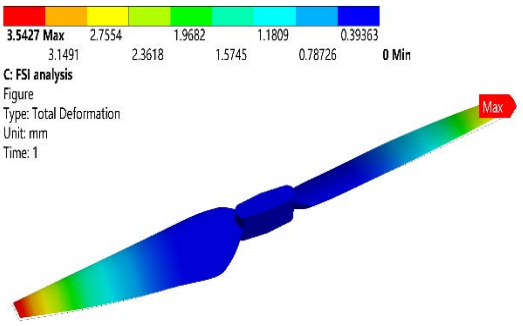

(a) Deformation distribution

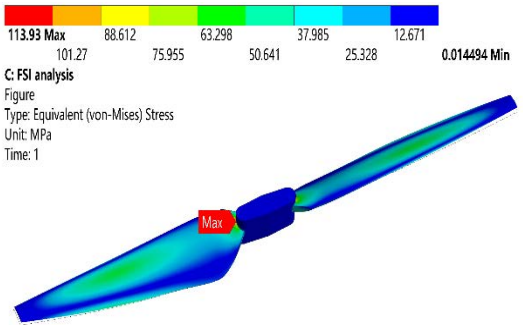

(b) Stress distribution

Fig. 11. Results of FSI analysis of the propeller design.

blades. A thick airfoil produces a low lift-drag ratio, which reduces the efficiency of the propeller. However, it has good aerodynamic characteristics to avoid stall. It can also be seen that the stress on the blade tip is relatively low. This indicates that a thinner airfoil design is preferable at this location. The maximum stress induced in the propeller is 113.95 MPa, which is far less than the allowable yield strength of the selected carbon fiber composite material. Thus, these results confirm the structural safety of the selected propeller design.

3.2 Structural stability analysis of the foldable arm

The foldable arm connects the propeller unit with the center frame. It is an important component as it transmits the propeller's force (lift) to the drone's central structure and payload. This section presents a comparison of the structural stability of the traditional metallic foldable arm with that of the foldable arm made using the novel lightweight carbon fiber composite material.

The deformation distribution of the foldable arms made of traditional aluminum alloy material and of carbon fiber composite material under the application of the same shear load is shown in Fig. 12. The end of the arm that is connected to the center frame is set as fixed, thus it shows a very small deformation. The maximum deformation in the two models appears at the end connected to the propeller assembly. The maximum deformation of the composite carbon fiber material foldable arm is 4.98 mm, which is more than double the deformation of the aluminum foldable alloy arm. However, this relatively higher

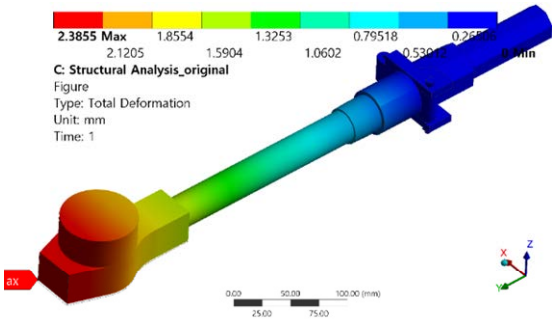

(a) Aluminum alloy foldable arm

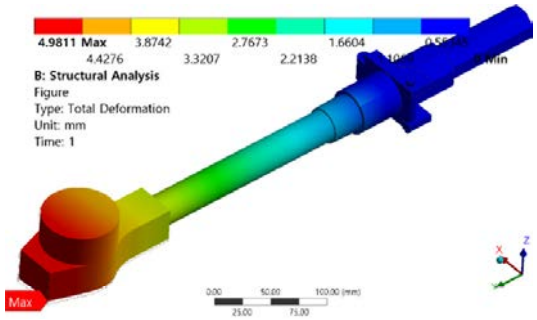

(b) Carbon fiber composite foldable arm

Fig. 12. Deformation distribution in the foldable arms made using two different materials.

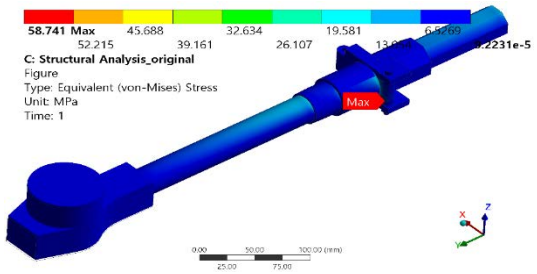

(a) Aluminum alloy foldable arm

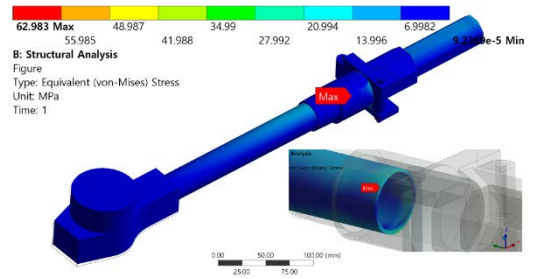

(b) Carbon fiber composite foldable arm

Fig. 13. Stress distribution in the foldable arms made using two different materials.

maximum deformation can be neglected considering the total length of the foldable arm. In addition, considering the elastic recovery ability of the carbon fiber composite material, the maximum deformation can be considered to be well within the acceptable range.

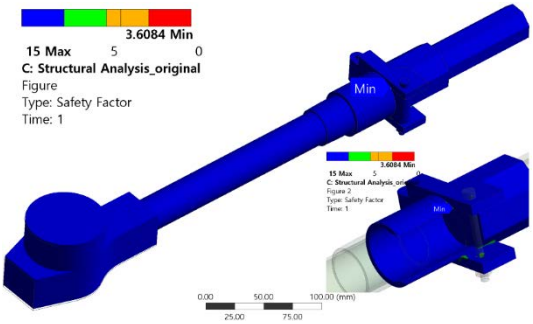

(a) Aluminum alloy foldable arm

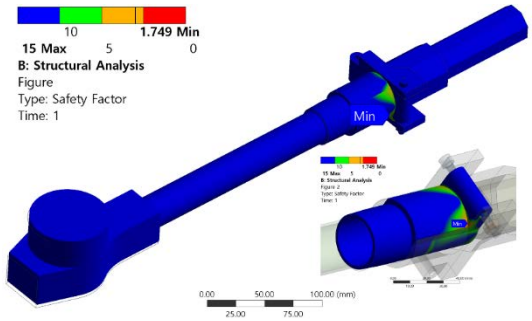

(b) Carbon fiber composite foldable arm

Fig. 14. Safety factor distribution in the foldable arms made using two different materials.

The stress distributions in the two foldable arms under the same boundary conditions are shown in Fig. 13. It can be seen that the maximum stress of 58.741 MPa appears at the hinge part of the aluminum alloy foldable arm. The maximum value of stress in the carbon fiber composite foldable arm does not differ greatly from that in the aluminum alloy arm. However, in the carbon fiber composite foldable arm, the maximum stress appears at the position where the carbon fiber rod connects to the hinge part.

The safety factor shown in Fig. 14 is obtained by calculating the quotient of the yield strength and the maximum stress of each component material. As predicted, the minimum safety factor of the aluminum alloy foldable arm appears at the hinge part that is made of plastic. The minimum safety factor of the composite foldable arm is located inside the socket of the hinge part in which the composite rod is inserted. This is due to the characteristics of repeated fold, the material of the inner part of the connecting part has to use the reinforced ABS plastic in the design. The minimum safety factor value of the composite material foldable arm is 1.75. Since the required safety factor has been accounted for in the applied load, a safety factor greater than 1.0 here satisfies the design requirements for structural stability.

4. Conclusions

The presented work consisted of a numerical investigation of the key structural and propulsion components of a hexarotor drone used for real-time fine dust monitoring. A series of aero-

dynamic simulations were carried out on eight different propeller designs using FVM, and structural stability analysis of the propellers and the foldable arm was carried out using FEM. The following conclusions have been drawn from the presented work:

1) The propeller with the maximum camber (C2) airfoil design can provide the greatest thrust but it requires more torque to operate. The differences in height between the starting point of the chord on the leading edge of airfoil and the reference plane (H1, H2, H3) have no significant effect on the propeller's propulsion performance and torque requirement. By comparing the influence of different distributions and magnitudes of airfoil twist angles, it can be concluded that a design with a slight offset of the maximum twist angle from the root to the blade tip can generate greater lift. Furthermore, the larger twist angle (W2) can provide 1.5 times greater thrust than the relatively smaller twist angle (W3). The correctness of these conclusions is verified through comparisons of the simulation results of multiple propeller designs.

2) Observation of the aerodynamic characteristics of the flow field on the selected optimal propeller design (design 2) showed that the pressure on the bottom surface of the blade is significantly higher than that on the top surface, and it shows a decreasing trend from the root of the blade to the tip. That is to say, the propulsion force of the propeller under the simulated working conditions is mainly produced in the middle and tip parts of the blade. There is a negative pressure on the upper side of the airfoil, which indicates that the blade is sucked up by the air flowing over the upper surface. The negative pressure generated on the top surface contributes more to the lift generated by the propeller.

3) Through the numerical analysis method of fluid-solid coupling, the structural safety of the carbon fiber propeller with high recovery elasticity was investigated. The maximum stress occurred at the root of the blade, which is the reason why a thicker airfoil is generally used at this part of the blade. A thicker airfoil produces a lower lift-drag ratio, which reduces the propulsion efficiency of the propeller. However, such a profile has better aerodynamic characteristics for stall avoidance. The stress appearing at the blade tip is relatively low, which indicates that a thinner blade shape is preferable at this part.

4) A comparison of the structural stability of the traditional aluminum alloy foldable arm and the novel carbon fiber composite foldable arm was also carried out. The smallest safety factor for both arm types was found to occur at the hinge. This a problem can perhaps be overcome through the incorporation of new composite materials in future foldable arm designs. However, the results of the numerical investigations showed that the presented foldable arm designed with carbon fiber composite material can meet the safety requirements for operation under the required working conditions.

Acknowledgments

This work was supported by the Regional Leading Research Center of NRF and MOCIE (NRF-2019R1A5A8083201). Y. T. Wu and Z. Qin contributed equally to this work.

References

[1] N. A. Khan, N. Z. Jhanjhi, S. N. Brohi, R. S. A. Usmani and A. Nayyar, Smart traffic monitoring system using unmanned aerial vehicles (UAVs), *Comput.Commun.*, 157 (2020) 434-443.

[2] S. Lee and K. Kwak, Assessing 3-D spatial extent of near-road air pollution around a signalized intersection using drone monitoring and WRF-CFD modeling, *International Journal of Environmental Research and Public Health*, 17 (2020).

[3] R. Song, G. Shen, Y. Liu, F. Tang, Q. Chen and P. Sun, Preparation and characterization of an oil-in-water microemulsion of thiamethoxam and acetamiprid without organic solvent for unmanned aerial vehicle spraying, *Colloids Surf. Physicochem. Eng. Aspects*, 607 (2020) 125485.

[4] J. K. Zégre-Hemsey, M. E. Grewe, A. M. Johnson, E. Arnold, C. J. Cunningham, B. M. Bogle and W. D. Rosamond, Delivery of automated external defibrillators via drones in simulated cardiac arrest: users' experiences and the human-drone interaction, *Resuscitation* (2020).

[5] Y. Liu, H. Dai, Q. Wang, M. K. Shukla and M. Imran, Unmanned aerial vehicle for internet of everything: opportunities and challenges, *Comput.Commun.*, 155 (2020) 66-83.

[6] H. Rodrigue, S. Cho, M. Han, B. Bhandari, J. Shim and S. Ahn, Effect of twist morphing wing segment on aerodynamic performance of UAV, *Journal of Mechanical Science and Technology*, 30 (1) (2016) 229-236.

[7] M. Hassanalian and A. Abdelkefi, Classifications, applications, and design challenges of drones: a review, *Prog. Aerospace Sci.*, 91 (2017) 99-131.

[8] F. Outay, H. A. Mengash and M. Adnan, Applications of unmanned aerial vehicle (UAV) in road safety, traffic and highway infrastructure management: recent advances and challenges, *Transportation Research Part A: Policy and Practice*, 141 (2020) 116-129.

[9] J. Song, Y. Byun, J. Jeong, J. Kim and B. Kang, Experimental study on cascaded attitude angle control of a multi-rotor unmanned aerial vehicle with the simple internal model control method, *Journal of Mechanical Science and Technology*, 30 (11) (2016) 5167-5182.

[10] N. T. B. Hoang, Computational investigation of variation in wing aerodynamic load under effect of aeroelastic deformations, *Journal of Mechanical Science and Technology*, 32 (10) (2018) 4665-4673.

[11] D. Han, D. Y. Gwak and S. Lee, Noise prediction of multi-rotor UAV by RPM fluctuation correction method, *Journal of Mechanical Science and Technology*, 34 (4) (2020) 1429-1443.

[12] G. Chang, H. R. Karbasian, S. Zhang, Y. Yan, B. Chen and K. C. Kim, The influence of kinematics of blades on the flow structure in deep dynamic stall, *Journal of Mechanical Science and Technology*, 34 (7) (2020) 2855-2868.

[13] J. Moon, C. Kim, Y. Youm and J. Bae, UNI-copter: a portable single-rotor-powered spherical unmanned aerial vehicle (UAV)

with an easy-to-assemble and flexible structure, *Journal of Mechanical Science and Technology*, 32 (5) (2018) 2289-2298.

[14] H. Cho, H. Ryu, S. J. Shin, I. Cho and J. Jang, Development of a coupled analysis regarding the rotor/dynamic components of a rotorcraft, *Journal of Mechanical Science and Technology*, 28 (12) (2014) 4841-4856.

[15] L. V. Campo, A. Ledezma and J. C. Corrales, Optimization of coverage mission for lightweight unmanned aerial vehicles applied in crop data acquisition, *Expert Syst. Appl.*, 149 (2020) 113227.

[16] V. Chamola, P. Kotesh, A. Agarwal, Naren, N. Gupta and M. Guizani, A comprehensive review of unmanned aerial vehicle attacks and neutralization techniques, *Ad Hoc Networks* (2020) 102324.

[17] J. González-García, R. L. Swenson and A. Gómez-Espinosa, Real-time kinematics applied at unmanned aerial vehicles positioning for orthophotography in precision agriculture, *Comput. Electron. Agric.*, 177 (2020) 105695.

[18] I. Gursul, D. J. Cleaver and Z. Wang, Control of low reynolds number flows by means of fluid-structure interactions, *Prog. Aerospace Sci.*, 64 (2014) 17-55.

[19] X. Li, K. Sun and F. Li, General optimal design of solar-powered unmanned aerial vehicle for priority considering propulsion system, *Chinese Journal of Aeronautics*, 33 (8) (2020) 2176-2188.

[20] E. Douvi, T. Athanasios and D. Margaris, Evaluation of the turbulence models for the simulation of the flow over a National Advisory Committee for Aeronautics (NACA) 0012 airfoil, *Journal of Mechanical Engineering Research*, 4 (2012).

[21] H. Zhu, H. Nie, L. Zhang, X. Wei and M. Zhang, Design and assessment of octocopter drones with improved aerodynamic efficiency and performance, *Aerospace Science and Technology*, 106 (2020) 106206.

[22] M. Hassanalian, M. Ashrafizaadeh, S. Ziaei-Rad and M. Radmanesh, A new method for design of fixed wing micro air vehicle, *Proc. of International Micro Air Vehicle 2012 Conference (IMAV2012)*, Braunschweig, Germany (2012).

[23] Z. Qin, Y. Wu, A. Huang, S. Lyu and J. Sutherland, Theoretical design of a novel vibration energy absorbing mechanism for cables, *Applied Sciences*, 10 (2020) 5309.

[24] M. Moshfeghi and N. Hur, Numerical study on the effects of a synthetic jet actuator on S809 airfoil aerodynamics at different flow regimes and jet flow angles, *Journal of Mechanical Science and Technology*, 31 (3) (2017) 1233-1240.

[25] Z. Qin, Y. T. Wu, A. Eizad, K. H. Lee and S. K. Lyu, Design and evaluation of two-stage planetary gearbox for special-purpose industrial machinery, *J. Mech. Sci. Technol.*, 33 (12) (2019) 5943-5950.

[26] Z. Qin, H. I. Son and S. K. Lyu, Design of anti-vibration mounting for 140A class alternator for vehicles, *J. Mech. Sci. Technol.*, 32 (11) (2018) 5233-5239.

[27] Z. Qin, Q. Zhang, Y. T. Wu, A. Eizad and S. K. Lyu, Experimentally validated geometry modification simulation for improving noise performance of CVT gearbox for vehicles, *Int. J. Precis. Eng. Manuf.*, 20 (11) (2019) 1969-1977.

[28] H. T. B. Ngoc, A numerical approach for assessing flow compressibility and transonic effect on airfoil aerodynamics, *Journal of Mechanical Science and Technology*, 34 (5) (2020) 2047-2053.

[29] J. Aurell, W. Mitchell, V. Chirayath, J. Jonsson, D. Tabor and B. Gullett, Field determination of multipollutant, open area combustion source emission factors with a hexacopter unmanned aerial vehicle, *Atmos. Environ.*, 166 (2017) 433-440.

[30] Z. Qin, Y. Wu, A. Eizad, S. Lyu and C. Lee, Advancement of mechanical engineering in extreme environments, *International Journal of Precision Engineering and Manufacturing-Green Technology* (2021).

[31] Q. Chen, X. Li, R. Song, H. Wang, B. Li, H. He and Z. Peng, Development and utilization of hexacopter unmanned aerial vehicle platform to characterize vertical distribution of boundary layer ozone in wintertime, *Atmospheric Pollution Research*, 11 (7) (2020) 1073-1083.

[32] Y. Liu, P. Li, W. He and K. Jiang, Numerical study of the effect of surface grooves on the aerodynamic performance of a NACA 4415 airfoil for small wind turbines, *J. Wind Eng. Ind. Aerodyn.*, 206 (2020) 104263.

[33] J. Chen, H. Yang, M. Yang, H. Xu and Z. Hu, A comprehensive review of the theoretical approaches for the airfoil design of lift-type vertical axis wind turbine, *Renewable and Sustainable Energy Reviews*, 51 (2015) 1709-1720.

[34] Y. Shi, J. Bai, J. Hua and T. Yang, Numerical analysis and optimization of boundary layer suction on airfoils, *Chinese Journal of Aeronautics*, 28 (2) (2015) 357-367.

[35] S. J. Stebbins, E. Loth, A. P. Broeren and M. Potapczuk, Review of computational methods for aerodynamic analysis of iced lifting surfaces, *Prog. Aerospace Sci.*, 111 (2019) 100583.

[36] Y. Wu, Z. Qin, A. Eizad and S. Lyu, Design and numerical simulation-based optimization of a novel flat-face coupling system for hydraulic power equipment, *Applied Sciences*, 11 (1) (2021).

[37] Y. Wu, Z. Qin, A. Eizad, S. Lyu and C. Lee, Numerical investigation of flow characteristics in a viscous damping system with symmetrical hydraulic cylinders, *International Journal of Precision Engineering and Manufacturing* (2021).

[38] L. Ping, B. Tang and S. Kaewunruen, Vibration-induced pressures on a cylindrical structure surface in compressible fluid, *Applied Sciences*, 9 (7) (2019) 1403.

[39] M. Akbay, C. Schroeder and T. Shinar, Boundary pressure projection for partitioned solution of fluid-structure interaction with incompressible dirichlet fluid domains, *Journal of Computational Physics*, 425 (2021) 109894.

[40] Z. Qin, Y. Wu, A. Eizad, N. Jeon, D. Kim and S. Lyu, A study on simulation based validation of optimized design of high precision rotating unit for processing machinery, *International Journal of Precision Engineering and Manufacturing*, 20 (9) (2019) 1601-1609.

[41] Z. Qin, Y. T. Wu and S. K. Lyu, A review of recent advances in design optimization of gearbox, *Int. J. Precis. Eng. Manuf.*, 19 (11) (2018) 1753-1762.

Yu-Ting Wu is a Ph.D. candidate in the Department of Mechanical and Aerospace Engineering, Gyeongsang National University. Her research interest is mechanical system design.

Zhen Qin is a Ph.D. candidate in the Department of Mechanical and Aerospace Engineering, Gyeongsang National University. He has worked at R&D Center of Kdac Co. Ltd., since 2013 and was awarded the title of excellent engineer. His primary research interest is mechanical system design.

Amre Eizad received the Ph.D. degree in Mechanical and Aerospace Engineering from Gyeongsang National University, Korea, in 2020. He is currently working as a Postdoctoral Researcher with the Intelligent Medical Robotics Laboratory, Gwangju Institute of Science and Technology, Korea.

Sung-Ki Lyu received his Bachelor's, Master's degrees at Chonbuk National University, Korea, in 1987, 1989, respectively, and got his Doctor's degrees at Tohoku University, Japan, in 1994. Dr. Lyu is currently a Professor of Gyeongsang National University in Jinju, Korea.